Acta Pharmaceutica Sinica B 2026;16(2):1074−1089

Chinese Pharmaceutical Association
Institute of Materia Medica, Chinese Academy of Medical Sciences

Acta Pharmaceutica Sinica B

www.elsevier.com/locate/apsb
www.sciencedirect.com

ORIGINAL ARTICLE

Biomimetic nitric oxide nanogenerators for synergistic gas-mild photothermal therapy of large solid tumor

Caixia Tan, Ming Yan, Xinping Luo, Honghao Sun, Zhanwei Zhou*, Minjie Sun*

NMPA Key Laboratory for Research and Evaluation of Pharmaceutical Preparations and Excipients, State Key Laboratory of Natural Medicines, Department of Pharmaceutics, China Pharmaceutical University, Nanjing 210009, China

Received 4 May 2025; received in revised form 18 July 2025; accepted 6 October 2025

KEY WORDS

Nitric oxide;
Autophagy inhibition;
Mild photothermal therapy;
Deep penetration;
Gas therapy;
Apoptosis;
Cell membrane;
Solid tumor

Abstract The mild photothermal therapy of solid tumors was still bottlenecked by the uneven temperature distribution in tumor tissue and the autophagy-mediated resistance. Here, we leveraged the ultrasmall size (approximately 0.32 nm) and autophagy inhibitory property of nitric oxide (NO) to overcome these limitations for enhanced gas-photothermal therapy of large tumors. An NO donor was loaded into mesoporous polydopamine and coated with tumor cell membranes for tumor-targeting delivery. The acid-triggered release of NO potently inhibited autophagy to block the pro-survival pathway of tumor cells. Besides, as a small-molecule gas, it diffused freely into deep regions and precisely eliminated the deep-seated tumor cells, resulting in approximately 90% tumor inhibition in the late-stage breast tumor model (>500 mm^3). The NO gas therapy shows great potential for complementing other therapeutics for the synergistic therapy of large solid tumors.

© 2025 The Authors. Published by Elsevier B.V. on behalf of Chinese Pharmaceutical Association and Institute of Materia Medica, Chinese Academy of Medical Sciences. This is an open access article under the CC BY-NC-ND license (http://creativecommons.org/licenses/by-nc-nd/4.0/).

*Corresponding authors.
E-mail addresses: zwzhou@cpu.edu.cn (Zhanwei Zhou), msun@cpu.edu.cn (Minjie Sun).

Peer review under the responsibility of Chinese Pharmaceutical Association and Institute of Materia Medica, Chinese Academy of Medical Sciences.

https://doi.org/10.1016/j.apsb.2025.11.009
2211-3835 © 2025 The Authors. Published by Elsevier B.V. on behalf of Chinese Pharmaceutical Association and Institute of Materia Medica, Chinese Academy of Medical Sciences. This is an open access article under the CC BY-NC-ND license (http://creativecommons.org/licenses/by-nc-nd/4.0/).

1. Introduction

Photothermal therapy (PTT), a minimally invasive antitumor therapy with demonstrated efficacy, has been widely studied[1-4]. Some of the studies have entered clinical trial stages[5-7]. However, local hyperthermia (over 52 °C) inevitably induces pain and irreversible damage to healthy tissues[8], thus reducing compliance and clinical utility. Subsequently, many researchers have turned to exploring safer mild PTT (below 45 °C)[9]. Although this approach significantly improves patient compliance, it comes at the expense of antitumor efficacy[10]. Two major obstacles restrict its application as an independent and effective antitumor therapy. First, continuous thermal stimulation at low temperatures could hardly eliminate tumor cells but instead induces autophagy, a self-protective mechanism that mediated photothermal resistance[11]. Second, the complex physiological environment of solid tumors restricts the uniform distribution of photothermal agents, resulting in an uneven and insufficient thermal effect[12-14]. Therefore, exploring adjuvant strategies that address these two challenges is expected to sensitize mild PTT.

Autophagy is a self-protective mechanism by which cells evade the risk of apoptosis by degrading their damaged organelles or abnormal proteins in the face of adverse conditions[15-17]. Mild PTT may cause mitochondrial damage[18-20], oxidative stress[21-24], and cytoskeletal damage in tumor cells[25], thereby inducing autophagy. Tumor cells subsequently evade the activation of the apoptotic pathway by degrading damaged mitochondria[26-28]. The autophagy-based pro-survival mechanism confers resistance to PTT[29], allowing more tumor cells to survive and creating opportunities for recurrence and metastasis. Consequently, the inhibition of autophagy has emerged as a promising strategy to sensitize mild PTT[30-32].

In gas therapies[33], nitric oxide (NO) is a highly reactive gaseous free radical with diverse physiological functions in several fields, such as vasodilation[34,35], antibacterial therapy[36,37], and antitumor therapy[38-40]. High doses of NO exhibit potent inhibitory effects on tumor cells[41,42]. With the rising heat of autophagy regulation, some researchers have reported that NO could block autophagy by inhibiting the formation of autophagosomes[43,44], indicating its potential to assist mild PTT. Moreover, benefiting from its lipophilicity and ultra-small size (0.32 nm), NO can diffuse freely into deep tumor regions where ordinary nanopreparations can hardly reach[45]. Furthermore, due to its role in promoting angiogenesis[34,35], NO may promote the penetration and accumulation of photothermal agents into tumors, thereby creating a positive feedback mechanism for the antitumor effect of mild PTT[46]. Motivated by these advantages of NO, we speculate that NO-based adjuvant strategies hold promise for enhancing antitumor efficacy in combination with other therapies.

In this work, we prepared a biomimetic NO nanogenerator (mP-NO@CM, Scheme 1). Mesoporous polydopamine with good photothermal conversion property was used as the photothermal carrier[47], enabling efficient loading of NO donors *via* its mesoporous structure and achieving effective therapeutic concentration of NO. The coated tumor cell membranes endowed NO with homologous targeting ability *in vivo*[48,49]. Coupled with the acid-responsive release of NO donors, tumor targeting and precise NO release could be achieved to avoid early leakage during circulation. The released NO inhibited thermal-induced autophagy and promoted tumor cell apoptosis, thereby blocking this pro-survival pathway. Meanwhile, NO diffused deeply and killed deep tumor cells directly, alleviating the insufficient local antitumor efficacy caused by uneven heat distribution. This study confirmed the antitumor effect of NO-assisted mild PTT, thus highlighting the broader application of NO-based gas therapy for treating large solid tumors.

2. Materials and methods

2.1. Materials

Dopamine hydrochloride (D103111, DA) and 1,3,5-trimethylbenzene (T105015, TMB) were purchased from the Aladdin Chemical Reagent Company (Shanghai, China). Rhodamine B (BD150358, RhB) was purchased from Bide Pharmatech Co., Ltd. (Shanghai, China). Polyethylene-polypropylene glycol (901701, F127, average Mñ12,500) and 2,3-diaminonaphthalene (88461, DAN) were purchased from Sigma−Aldrich (St. Louis, Missouri, USA). Ammonium hydroxide solution (A801005, 25%−28%) was purchased from Macklin (Shanghai, China). Diethylenetriamine NONOate (GC18259, DETA NONOate) was purchased from GlpBio Technology (Montclair, California, USA). Chloroquine (HY-17589A, CQ) was purchased from MedChemExpress (Elizabeth, New Jersey, USA). Nitric Oxide assay kit (S0021S), BCA protein assay kit (P0012), 1,1′-dioctadecyl-3,3,3′,3′-tetramethylindocarbocyanine perchlorate (C1036, DiI), 3,3′-dioctadecyloxacarbocyanine perchlorate (C1038, DiO), 4′,6-diamidino-2-phenylindole (C1005, DAPI), thiazolyl blue tetrazolium bromide (ST316, MTT), calcein-AM (C2015M) and propidium iodide (C2015M, PI) were purchased from Beyotime Biotechnology (Shanghai, China). Annexin V-FITC/PI apoptosis detection kit (C8043-50T) was purchased from Titan Scientific Co., Ltd. (Shanghai, China). Lysotracker Green (KGE2209-200), Lysotracker Red (KGE2207-50), Dulbecco's modified Eagle's medium (KGL1206-500, DMEM), and Trypsin-EDTA (KGL2101-100) solution were purchased from KeyGEN Biotech (Jiangsu, China). DAF-FM DA (MA0200) was purchased from Meilunbio (Dalian, China). Cy5.5-NHS (D10013-1) and Cy3.5-NHS (D10011-1) were purchased from Duofluor (Shanghai, China). All other reagents and materials were purchased from the Servicebio Technology Co., Ltd. (Wuhan, China).

2.2. Cell culture and animals

4T1 cells (mouse breast cancer cells), luciferase-expressed 4T1 cells (4T1-luc), B16F10 cells (mouse melanoma cells), and RAW264.7 cells (mouse macrophage cells) were all cultured in DMEM containing 1% penicillin/streptomycin (Pen-Strep) with 10% FBS in the CO_2 incubator (Thermo Fisher, 50162972, USA) at 37 °C with 5% CO_2. The female BALB/c (6−8 weeks) mice were purchased from Huachuang Sino Pharmatech Co., Ltd. (Jiangsu, China). All animal experiments followed the regulations of the Institutional Animal Care and Use Committee of China Pharmaceutical University (Approval No. SYXK2021-0011) and the Science and Technology Department of Jiangsu Province approved protocols.

2.3. Synthesis and characterization of mPDA

Mesoporous polydopamine (mPDA) nanoparticles were prepared using the soft-template method[50]. F127 (0.1 g) was dissolved in 10 mL of water-ethanol mixture (v/v = 1:1). TMB (0.15 mL) was

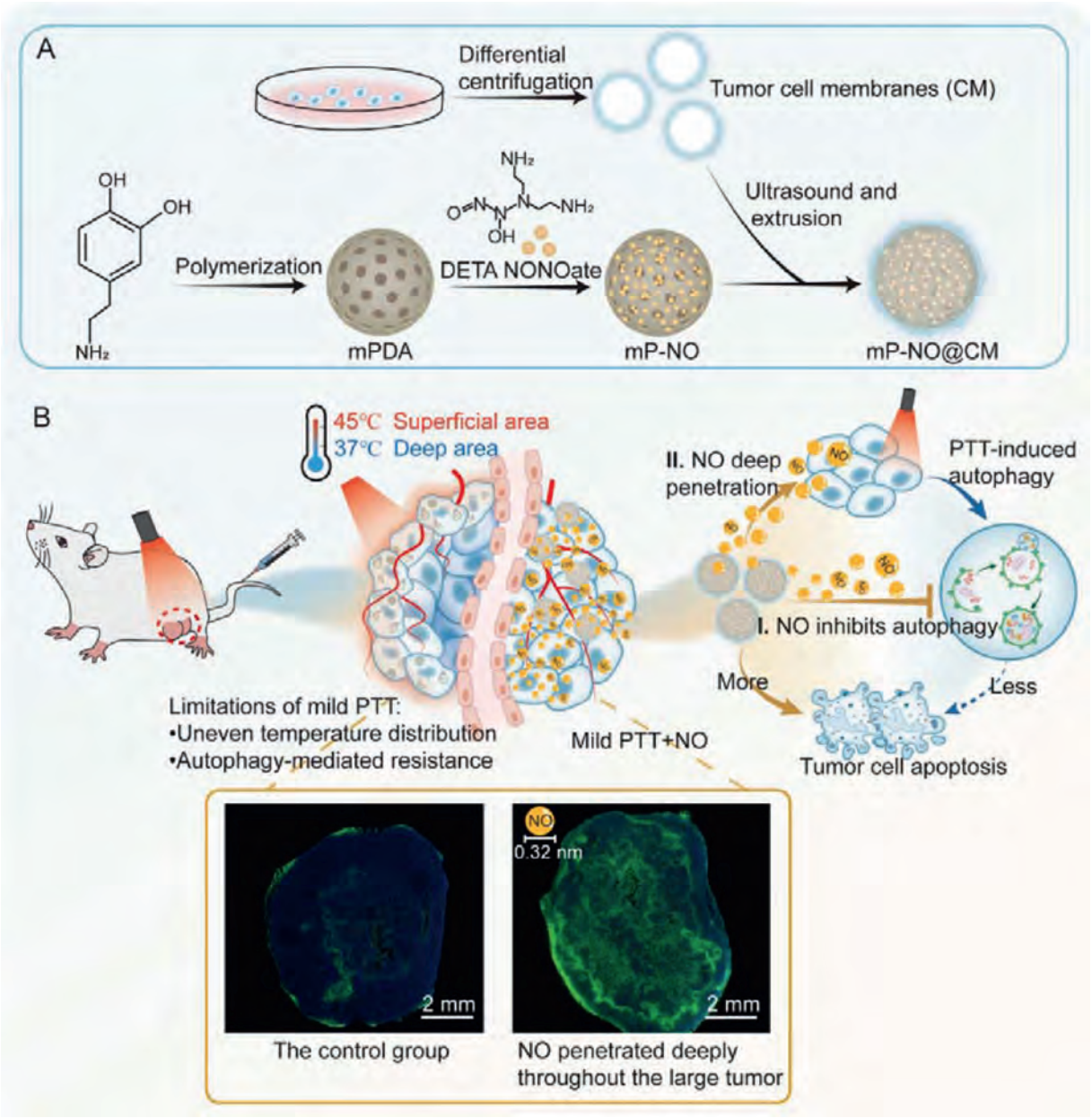

Scheme 1 Illustration of the preparation of NO nanogenerator (mP-NO@CM) and the mechanism of NO-based gas-photothermal therapy in solid tumors. (A) Procedures for preparing mP-NO@CM. (B) The mechanism of NO-assisted mild photothermal therapy *in vivo*. I. Mild PTT tends to induce pro-survival autophagy, which can be inhibited by NO, thereby promoting more tumor cells to apoptosis. II. NO can penetrate deeply into the tumor and exert an antitumor effect directly to compensate for the uneven and insufficient thermal effect in deep tumor regions.

added slowly under stirring to form a white emulsion. DA (50 mg) was added to the emulsion. Ten minutes later, aqueous ammonia (150 μL) was added dropwise. After 4 h of reaction, the precipitate was collected by centrifugation (D1524R, DLAB, Beijing, China) at 9000 rpm for 10 min, washed alternately with ethanol-acetone mixture (v/v = 2:1) and deionized water. Finally, the precipitate was collected and lyophilized to obtain mPDA. Its structure was confirmed by Fourier transform infrared spectroscopy (FT-IR, TENSOR27, Bruker, Germany). The hydrodynamic particle size and zeta potential were measured using Zeta Plus (Zetasizer Nano S90, Malvern, UK). The morphology was observed by transmission electron microscope (TEM, H-600, Hitachi, Japan) and scanning electron microscopy (SEM, Sigma 300, Zeiss, Germany). The isothermal adsorption and desorption curve was measured by the nitrogen adsorption method. The mesoporous size was analyzed using the Barrett-Joiner-Halenda model[51], and the specific surface area was calculated according to BET theory[52].

2.4. *Extraction and characterization of 4T1 cell membranes*

4T1 cell membranes were extracted by pretreatment with hypotonic solution and gradient centrifugation. Briefly, 4T1 cells were harvested and resuspended in Tris-Mg hypotonic solution (10 mmol/L KCl, 2 mmol/L $MgCl_2$, and 20 mmol/L Tris-HCl, pH 7.4). After standing at 4 °C for 12 h, the cells were homogenized using a cell ultrasonicator (Biosafer650-92, China). 4T1 cell

membranes were then extracted by gradient centrifugation (DLAB), and protein content was determined by BCA assay.

2.5. Preparation and characterization of nanoparticles

Preparation of NO-loaded mPDA (mP-NO): Mix DETA NONOate solution (final concentration of 200 μg/mL) with mPDA solution (final concentration of 1 mg/mL) and incubate at room temperature for 4 h. mP-NO nanoparticles were obtained by centrifugation and PBS washing.

Preparation of membrane-coated mPDA (mP@CM): Cell membranes (3 mg, calculated on protein content) were added to 1 mL of mPDA solution (1 mg/mL), and they were mixed by ultrasound for 3 min (ultrasonic power 80 W, 1 s on and 2 s off). Then, the liposome extruder was used to extrude the mixture, which was successively extruded through polycarbonate membranes from 400 to 200 nm 10 times to obtain mP@CM nanoparticles.

Preparation of membrane-coated mP-NO nanoparticles (mP-NO@CM): After mixing mP-NO solution with cell membranes, mP-NO@CM was obtained following the same procedures as mP@CM.

For characterization, the morphology of mP-NO@CM was photographed by TEM (Hitachi). The particle size and zeta potential were detected using Zeta Plus (Malvern). The particle size changes of mP-NO and mP-NO@CM in PBS at 4 °C and PBS containing FBS (5%, 10%, 15%) at 37 °C were monitored for several days.

2.6. Characterization of membrane-coated nanoparticle

Sodium dodecyl sulfate-polyacrylamide gel electrophoresis (SDS-PAGE) was performed to detect whether the cell membrane was successfully coated, and the results were compared with the free tumor cell membrane and mP-NO.

To further confirm the cell membranes' adsorption, the fluorescence colocalization of the carrier and the cell membrane was photographed by the confocal laser scanning microscope (CLSM, LSM 800, Zeiss, German). RhB (5 μg/mL) and mPDA (200 μg/mL) were mixed in the dark for 4 h. RhB-labeled mPDA (mP-RhB) was collected by centrifugation. It was then resuspended in PBS and co-extruded with 4T1 cell membrane to obtain mP-RhB@CM, to which 1 μL of DiO dye was added and then incubated at 37 °C for 30 min. The free dye was removed by PBS washing and centrifuged to obtain DiO-labeled mP-RhB@CM. 5×10^4 4T1 cells were seeded in confocal dishes and cultured for 24 h. Then, mP-RhB@CM-DiO (200 μg/mL) diluted in DMEM was added to the dishes and incubated for 3 h, after which the cells were washed with PBS three times. Finally, fluorescence colocalization was photographed by CLSM (Zeiss), and the images were then analyzed by Image J (National Institutes of Health, USA).

2.7. Drug loading detection

The content of DETA NONOate was detected by the DAN fluorescent probe, which can specifically detect NO in solution. DETA NONOate dissociated in the acidic reaction solution of DAN and was released in the form of NO. Therefore, there was a certain coefficient correlation between the content of DETA NONOate and NO measured by the DAN method, which required conversion. First, DAN was dissolved in 0.62 mol/L hydrochloric acid to prepare a 0.31 mmol/L solution. 10 μL of DAN solution was mixed with 100 μL of $NaNO_2$ standard solution (0−10 mmol/L) and reacted at room temperature for 10 min, then 5 μL of NaOH (2.8 mol/L) was added. After dilution with water, the fluorescence intensity was measured by a fluorescence spectrophotometer (Shimadz RF-6000, Japan), and a standard curve was drawn. The mP-NO solution was centrifuged (DLAB) to collect the supernatant 1, and the precipitate was resuspended and co-extruded with the cell membrane to obtain mP-NO@CM solution, which was centrifuged again to collect the supernatant 2. Mix the supernatants with the DAN solution separately to get the content of the unloaded drug. Next, the fluorescence intensity corresponding to the fed DETA NONOate (200 μg/mL) was measured using the same method, and then the NO content corresponding to the fed DETA was obtained after replacing the standard curve, which was regarded as the converted DETA feeding content. Then, it was substituted into the following Eqs. (1) and (2) to calculate the encapsulation efficiency and loading capacity of DETA NONOate in mP-NO@CM.

$$\text{Encapsulation efficiency}\,(\%) = \frac{\text{Weight of fed drug} - \text{Weight of unloaded drug}}{\text{Weight of fed drug}} \times 100 \quad (1)$$

$$\text{Loading capacity}\,(\%) = \frac{\text{Weight of fed drug} - \text{Weight of unloaded drug}}{\text{Weight of whole nanoparticles}} \times 100 \quad (2)$$

Furthermore, in order to investigate the binding force between DETA NONOate and mPDA, different reagents were used to compete for binding. NaCl (100 mmol/L), urea (100 mmol/L), and Triton X-100 (10%) were used to disrupt electrostatic binding, hydrogen bonding, and hydrophobic interaction, respectively. Briefly, mP-NO and mP-NO@CM were prepared and suspended with deionized water, NaCl, urea, and Triton X-100. After incubation at 37 °C for 4 h, the supernatant was diluted twice and added to the DAN assay solution for 15 min. The fluorescence intensity at 365 nm/450 nm was measured, representing the NO content released from the nanoparticles. The deionized water group was used as a control to analyze the main force affecting NO loading.

2.8. Photothermal properties of mP-NO@CM

A series of solutions of mP-NO@CM were prepared with concentrations of 50, 100, 200 and 400 μg/mL. And PBS was treated as a blank control. 200 μL of the above solutions were added into 96-well plates and irradiated with 808 nm laser (2 W/cm^2) for 5 min. The temperature was recorded every 30 s.

200 μL of mP-NO@CM solution (200 μg/mL) was added into a 96-well plate and continuously irradiated with 808 nm laser (2 W/cm^2) for 5 min. The laser was turned off, and the solution was allowed to return to room temperature and irradiated again for another 5 min. The cycle was repeated four times, during which the temperature was recorded every 1 min. Besides, the morphology of mP-NO@CM irradiated with an 808 nm laser for 10 min (2 W/cm^2) was also photographed by TEM (Hitachi).

mP-NO@CM (200 μg/mL) was exposed to laser irradiation for 5 min with a power density of 2 W/cm^2. Then, it was allowed to

cool to room temperature. The temperature changes were recorded every 30 s using a high-sensitive RTD thermometer. The photothermal conversion efficiency (η) of mP-NO@CM was calculated according to Eq. (3)[11].

$$\eta = \frac{hS(T_{max} - T_r) - Q_b}{I\left(1 - 10^{-A_{808}}\right)} \quad (3)$$

where h is heat transfer coefficient, S means the surface area of the sample container, T_{max} is the maximum temperature of the solution after laser irradiation, T_r is the room temperature, Q_b is the baseline energy of the sample of container, I is the laser power density (2 W/cm^2), and A808 means the absorbance of mP-NO@CM at 808 nm detected by UV−VIS spectrophotometer (UV-1800PC, MAPADA, China). Among these parameters, hS could be calculated by Eq. (4)[53].

$$\tau = \frac{m_s C_s}{hS} \quad (4)$$

where m_s and C_s are the mass (1.0 g) and heat capacity (4.2 J/g) of the deionized water, respectively. τ could be determined by the linear curve fitting of temperature cooling time *versus* its $-\mathrm{Ln}(\Delta T/\Delta T_{max})$.

2.9. Release of NO in different pH in vitro

mP-NO@CM was dissolved in phosphate buffer with different pH values, including pH 7.4, pH 6.5, and pH 5.0, to simulate the physiological environment, tumor microenvironment, and intracellular lysosomes, respectively. The samples were placed in a constant temperature shaker and shaken continuously (100 rpm, 37 °C). Then, they were taken out at specific time points (0, 0.5, 1, 2, 3, 4, 6, and 12 h), centrifuged, and the NO concentration in the supernatant was detected using the DAN method. The precipitate was resuspended with a buffer of the same pH and continued to be shaken at a constant temperature.

2.10. Homologous cell uptake

4T1 cells were seeded in 12-well plates at a density of 5×10^4 cells per well for 24 h and then incubated with free RhB (2.5 μg/mL), mP-RhB (200 μg/mL, containing about 2.5 μg/mL RhB), mP-RhB@CM (200 μg/mL, containing about 2.5 μg/mL RhB) for 2 h, respectively. Free preparations were removed by washing three times with PBS, then cells were harvested. Analysis was performed using a flow cytometer (BD FACSCelesta, USA).

To further examine the homologous targeting ability of the membrane-coated preparations, the uptake of mP-RhB and mP-RhB@CM (encapsulating 4T1 cell membranes) was compared in 4T1 cells, B16F10 cells, and RAW264.7 cells. The experimental protocols were performed as described above, and CLSM (Zeiss) was used for observation.

2.11. Cytotoxicity and apoptosis

The cytotoxicity of different preparations was detected by MTT assay. In brief, 4T1 cells were seeded in 96-well plates at a density of 5000 cells per well. After 24 h of culture, the cells were treated with PBS ± L, free NO ± L (DETA NONOate, 60 μmol/L), mP@CM ± L (200 μg/mL), and mP-NO@CM ± L (200 μg/mL), respectively (±L meant with or without laser, 808 nm, 2 W/cm^2, 3 min). After culturing for 24 h, MTT solution (0.5 mg/mL) was added and incubated for another 4 h, followed by DMSO solution and shaking for 15 min. Absorbance at 490 nm was measured using a microplate reader (Infinite F50, Tecan, Switzerland), and the cell viability was calculated.

For the apoptosis assay, 4T1 cells were seeded at a density of 5×10^4 cells per well in 12-well plates and treated with PBS ± L, mP@CM + L (200 μg/mL), and mP-NO@CM ± L (200 μg/mL), respectively (±L meant with or without laser, 808 nm, 2 W/cm^2, 3 min). After 24 h, Annexin V-FITC and PI staining were performed according to the instructions of the apoptosis kit. Then, cell apoptosis was examined by flow cytometry (BD).

2.12. Detection of intracellular NO generation

The intracellular NO content was measured using the Griess method. Simply, 4T1 cells were seeded at a density of 5×10^4 cells per well in 12-well plates and treated with PBS ± L, mP@CM ± L (200 μg/mL), and mP-NO@CM ± L (200 μg/mL), respectively. Then, the cells were lysed to quantify NO according to the instructions of the assay kit. Finally, the absorbance at 490 nm was measured using a microplate reader (Tecan).

2.13. The mechanism of intracellular NO release

4T1 cells were seeded in confocal dishes at a 5×10^4 cells/well density, treated with mP-NO@CM (200 μg/mL), and incubated for 2 or 5 h, respectively. After that, the plates were washed with PBS, and the NO probe DAF-FM DA (5 μmol/L) was added and incubated for 30 min. After washing, Lysotracker Red (5 μmol/L) was used to label lysosomes. Finally, the NO distribution in the cells was observed by CLSM (Zeiss), and the colocalization of NO and lysosomes was analyzed by calculating Pearson's correlation coefficient.

In another test, 4T1 cells were treated with mP-RhB@CM (200 μg/mL, with RhB 2.5 μg/mL) for 2 or 6 h, respectively, followed by washing with PBS and labeling with Lysotracker Green (5 μmol/L). Finally, the lysosomal escape of mP-RhB@CM was analyzed by CLSM (Zeiss) and compared with that of mP-NO@CM.

2.14. Imaging of NO permeation on 4T1 tumor spheroids

The tumor spheroid model was constructed to evaluate the deep penetration of NO released from mP-NO@CM. First, 4T1 cells were seeded at a density of 2000 cells per well in ultra-low-adsorption U-bottom 96-well plates and cultured for 6 days to form dense spheroids. They were treated with PBS, mP@CM (200 μg/mL, DiI labeled), or mP-NO@CM (200 μg/mL, DiI labeled) for 4 h, respectively. Following PBS washing, DAF-FM DA solution (5 μmol/L) was added to track NO in the spheroids. After 30 min of incubation, the spheroids were transferred carefully to a confocal dish and viewed under the 20 × objective of CLSM (Zeiss).

2.15. Antitumor effects on 4T1 tumor spheroids

4T1 tumor spheroids were established as described in 2.14. When the diameter of spheroids exceeded 400 mm (Day 0), different treatments were given (PBS ± L, mP@CM ± L, mP-NO@CM ± L). And the concentration of mP@CM and mP-NO@CM was 200 μg/mL. After incubation for 12 h, tumor spheroids were exposed to laser irradiation (808 nm, 2 W/cm^2, 3 min). Subsequently, they were photographed by an inverted

fluorescence microscope on Days 1, 3, 5, and 7. The maximum diameter (d_{max}) and minimum diameter (d_{min}) were determined by Image J. Then the volume of tumor spheroids was calculated ($V = {d_{min}}^2 \times d_{max}/2$). The volume change ratio was calculated according to Eq. (5)[54]:

$$\text{Change ratio}\ (\%) = \frac{V_{D7}}{V_{D0}} \times 100 \quad (5)$$

where V_{D7} and V_{D0} meant the volume on Day 7 and Day 0, respectively.

Besides, the cell viability of the tumor spheroids was also investigated by live/dead staining. Briefly, tumor spheroids on Day 2 were stained with calcein-AM (2 μmol/L) and PI (7.5 μmol/L) and incubated at 37 °C for 20 min. Then, they were observed under the 10 × objective by fluorescence imaging (Nikon Ts2R, Japan).

2.16. Inhibitory effect of mP-NO@CM on autophagosomes

4T1 cells were seeded in confocal dishes at a density of 5×10^4 cells per dish and treated with PBS ± L, mP@CM ± L (200 μg/mL), and mP-NO@CM ± L (200 μg/mL, 808 nm, 2 W/cm^2, 3 min). After that, MDC dye (5 μmol/L) was used to label autophagosomes or autolysosomes. The intracellular fluorescent spots were observed by CLSM (Zeiss) and counted by Image J.

2.17. Western blot assay

In vitro cellular samples: In brief, 4T1 cells were seeded in 6-well plates at a density of 1×10^5 cells per well and cultured for 24 h before treatments with PBS, PBS + L, mP@CM + L (200 μg/mL), mP-NO@CM (200 μg/mL), and mP-NO@CM + L (200 μg/mL). After 12 h of incubation, the cells were washed with PBS and lysed with RIPA lysate (containing 1% PMSF and 1% protease inhibitor) for 45 min on ice. The cells were collected and centrifuged (DLAB) at 12,000 rpm for 15 min to extract proteins. Afterward, protein quantification was performed using the BCA assay kit. The remaining protein sample was mixed with 5 × loading buffer and boiled for 5 min. SDS-PAGE electrophoresis was then performed. The membranes were transferred (0.22 μm PVDF membrane), blocked (5% BSA), and incubated overnight at 4 °C with primary antibodies for LC3 (1:1000 dilution) and β-actin (1:3000 dilution). The next day, the HPR-labeled secondary antibody (1:5000 dilution) was incubated at room temperature for 1 h. After 30 min of washing, the bands were observed by gel imager (Tanon 2500R, China), and the bands were semi-quantified using image J.

Ex vivo tumors: The collected tumors were rinsed with precooled PBS, quickly weighed, and put into grinding tubes. RIPA lysate (1 mg of tumor corresponding to 100 μL of lysate) and steel grinding balls (diameter of 3 mm) were added. The tumors were fully ground with a frozen grinding instrument (Jingxin JXFSTPRP-CL-24, China) (frequency 60 Hz, run for 30 s and stop for 45 s, repeated 5 times). Afterward, proteins were extracted and electrophoresed following the same procedures described above. Finally, the bands were viewed and semi-quantified.

2.18. Efficacy of autophagy inhibitors in combination with mild PTT

MTT assay and calcein-AM/PI staining were used to evaluate the necessity of autophagy inhibitors combined with mid PTT. CQ was selected as a model autophagy inhibitor. For the MTT assay, 4T1 cells were treated with PBS ± L, CQ ± L (25 μmol/L), mP@CM ± L (200 μg/mL), mP@CM + CQ ± L (200 μg/mL, CQ 25 μmol/L), and mP-NO@CM ± L (200 μg/mL), respectively. The laser condition was the same as before. The MTT assay was then performed as described above.

For the live/dead staining assay, 4T1 cells were seeded at a density of 5×10^4 cells per well in 24-well plates and treated with PBS ± L, CQ ± L (25 μmol/L), mP@CM ± L (200 μg/mL), mP@CM + CQ ± L (200 μg/mL, CQ 25 μmol/L), mP-NO@CM ± L (200 μg/mL) for 24 h. The laser irradiation was initiated 12 h after administration (2 W/cm^2, 5 min). Cells were then stained with calcein-AM (2 μmol/L) and PI (7.5 μmol/L) and incubated at 37 °C for 20 min. After washing with PBS, red or green fluorescence was observed under an inverted fluorescence microscope (Nikon).

2.19. Hemolysis test of mP-NO@CM

Blood was collected from mice using EDTA-anticoagulated tubes. Plasma was removed by centrifugation at 3000 rpm for 10 min, and the collected erythrocytes were resuspended with different concentrations of mP-NO@CM (25, 50, 100, 200 and 400 μg/mL). PBS and deionized water were used as negative and positive controls. After standing at 37 °C for 1 h, the cells were centrifuged at 3000 rpm for 10 min, and the hemolysis of each group was observed.

2.20. Biodistribution of mP-NO@CM in vivo

BALB/c mice were subcutaneously injected with 4×10^6 4T1 cells. Free Cy5.5, mP-Cy5.5, and mP-Cy5.5@CM (Cy5.5, 0.5 mg/kg) were intravenously injected when the tumor grew to 150 mm^3. At 4, 6, 10, 24, and 36 h, the distribution of the preparations *in vivo* was imaged by a small animal imager (TanonABLX6, China). The mice were sacrificed at 36 h. The tumors and major organs (heart, liver, spleen, lung, and kidney) were collected and imaged.

2.21. Antitumor efficacy in the 4T1 early-stage breast tumor model

The 4T1-luc breast cancer model was established to evaluate the antitumor effect *in vivo*. In brief, 4T1-luc cells (1×10^6 cells per mouse) were inoculated into the fat pads of BALB/c mice. When the tumor volumes grew to 100 mm^3, the mice were randomly divided into five groups ($n = 8$) and given different treatments: saline, saline + L, mP@CM + L (15 mg/kg), mP-NO@CM (15 mg/kg), and mP-NO@CM + L (15 mg/kg). Specifically, the above preparations were intravenously injected on Days 2, 5, and 8, followed by 808 nm laser irradiation (2 W/cm^2, 5 min) 12 h later. The tumor volume ($V = \text{width}^2 \times \text{length}/2$) and body weight were detected every two days, and the tumor growth trend was monitored by the bioluminescence imaging system on Days 1, 8, and 16. The mice were then sacrificed, and the tumors were collected for Western blot, LC3 immunofluorescence staining, p62 immunofluorescence staining, TUNEL apoptosis staining, and H&E staining.

2.22. Antitumor efficacy in the 4T1 late-stage breast tumor model

The late-stage breast tumor model was established to evaluate the permeation of NO in large solid tumors. Briefly, 4T1 cells (1×10^6 cells per mouse) were subcutaneously inoculated into the right lower abdomen of BALB/c mice, and the mice were randomly divided into five groups ($n = 8$). When tumor volumes

increased to 450−500 mm^3, different treatments were given: saline, saline + L, mP@CM + L (15 mg/kg), mP-NO@CM (15 mg/kg), mP-NO@CM + L (15 mg/kg, 808 nm, 2 W/cm^2, 5 min). The specific experimental procedures were the same as described previously. Of note, to visualize intratumor penetration of the preparations, the nanoparticles were labeled with Cy3.5-NHS (0.5 mg/kg). Tumors were collected 12 h after intravenous administration, embedded in OCT, frozen in liquid nitrogen, and sectioned into slides. The slides were stained with DAF-FM DA (100 μmol/L) and DAPI. Finally, the fluorescence distribution in tumor sections was visualized. At the end of the treatments, the tumors were collected and cut into superficial layers (approximately 3 mm wide area from the edge to the inside) and deep layers, which were ground and digested into single-cell suspension, respectively. Annexin V-FITC/PI staining was performed using flow cytometry (BD). Finally, other collected tumors were fixed with paraformaldehyde and subjected to H&E, CD31 immunofluorescence staining, and TUNEL staining.

2.23. *Biocompatibility evaluation in vivo*

Healthy mice were randomly divided into two groups ($n = 3$) and received injections of saline or mP-NO@CM (15 mg/kg) *via* the tail vein three times. Blood samples were then collected for routine blood tests and blood biochemical tests. Meanwhile, the major organs (heart, liver, spleen, lung, and kidney) were also collected for H&E staining analysis.

2.24. *Statistical analysis*

All data are representative of at least three independent replicate experiments and are presented as mean ± SD. Student's *t*-test was used to compare two groups, and ordinary one-way ANOVA was used to compare three or more groups. The survival time of mice was recorded and analyzed using the log-rank test. The statistical significance of the results was shown as the following: $*P < 0.05$, $**P < 0.01$, $***P < 0.001$, $****P < 0.0001$. All statistical analyses were performed by GraphPad Prism 6.01.

3. Results and discussion

3.1. *Preparation and characterization of mP-NO@CM*

Mesoporous polydopamine (mPDA) was prepared using the previous method[50]. The structure was confirmed by Fourier transform infrared spectrum scanning (Supporting Information Fig. S1). Simply, mPDA exhibited a broad absorption band at 3500−3100 cm^{-1}, which represented the stretching vibration of the intermolecular O−H bond and the secondary amine N−H bond Meanwhile, the peak at 1615 cm^{-1} indicated the bending vibrations of the secondary amine N−H bond. A multi-peak structure of an aromatic ring was observed at 1600−1450 cm^{-1}. Besides, the stretching vibrations of the aromatic amine C−N bond (1240 cm^{-1}) and the phenolic C−O bond (1042 cm^{-1}) were observed. The attribution of the above

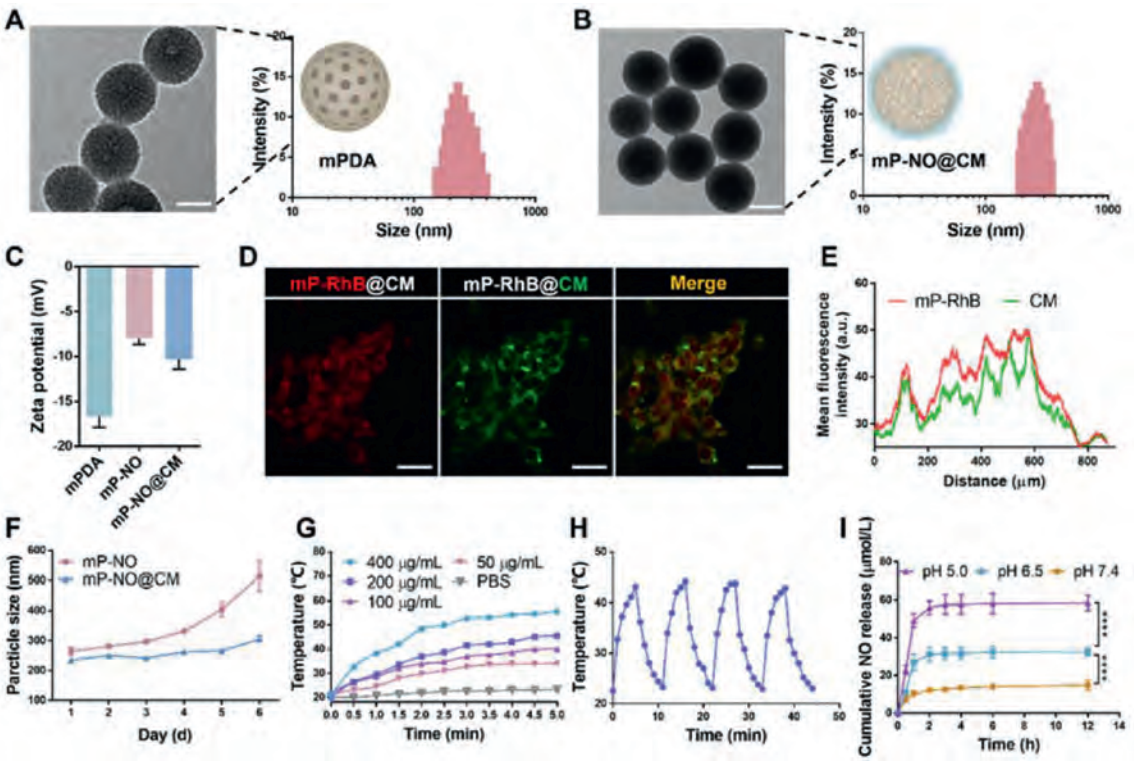

Figure 1 Characterization and photothermal performance of mP-NO@CM. (A, B) Representative TEM image and particle size distribution of (A) mPDA and (B) mP-NO@CM. Scale bars, 100 nm. (C) Zeta potential, $n = 5$. (D) Confocal images of colocalization of mP-RhB (Red) and the coated cell membranes labeled with DiO (Green). Scale bars, 40 μm. (E) Fluorescence colocalization analysis of Fig. 1D. (F) Particle size variations of mP-NO and mP-NO@CM, $n = 3$. (G) Temperature rising profile of mP-NO@CM with different concentrations under 808 nm laser (2 W/cm^2). (H) Photothermal stability of mP-NO@CM. (I) Cumulative NO release under different pH values, $n = 3$. Data are presented as mean ± SD, $****P < 0.0001$.

characteristic peaks proved the presence of dopa-indole skeleton, which was typical of successful dopamine polymerization[55]. For the morphology study, mPDA exhibited a spherical shape with a porous structure under transmission electron microscopy (TEM) and scanning electron microscopy (SEM) (Fig. 1A and Supporting Information Fig. S2). DETA NONOate, a NO donor with cationic amino groups, can be loaded on mPDA *via* electrostatic interaction and hydrogen bonding to form mP-NO (Supporting Information Fig. S3). Then, 4T1 cell membranes were coated on the surface of mP-NO to obtain mP-NO@CM. The intact membrane coating layer can be clearly seen under TEM. The general particle size was homogeneous at 226.3 ± 1.8 nm (Fig. 1B). The zeta potential was stabilized at −10.3 ± 1.1 mV (Fig. 1C). In addition, the rhodamine B (RhB)-labeled mPDA and DiO-labeled cell membranes showed apparent colocalization under confocal microscopy (Fig. 1D and E). The result of SDS-PAGE also revealed the successful coating of cell membranes (Supporting Information Fig. S4). Benefiting from the membrane coating, mP-NO@CM had better colloidal stability, serum stability, and hemocompatibility, which supported the intravenous administration (Fig. 1F, Supporting Information Figs. S5 and S6). Moreover, the photothermal properties and photothermal stability were not affected (Fig. 1G and H). It showed a relatively high photothermal conversion efficiency of about 42.9% and kept an intact mesoporous spherical structure after laser irradiation (Supporting Information Figs. S7 and S8).

The amount of NO released *in vivo* depends on the NO donor loaded *in vitro*. The pore size of mPDA was mainly dispersed in the mesoporous range of 2−50 nm, among which the most probable pore size was about 7 nm. The total pore volume was about 0.1 cm^3/g. The specific surface area was about 25.7 m^2/g (Supporting Information Fig. S9). Based on structural advantages, the encapsulation efficiency and drug loading capacity of mP-NO@CM were calculated to be 54.9 ± 1.8% and 11.7 ± 1.4%, respectively, which were significantly higher than those of non-mesoporous nP-NO@CM (25.5 ± 3.4% and 4.6 ± 0.2%) (Supporting Information Fig. S10). In order to study the release of NO, the cumulative release curves in phosphate buffer at pH 7.4, pH 6.5, and pH 5.0 were recorded. As shown in Fig. 1I, NO was partially released in a pH 6.5 medium, which mimicked the tumor

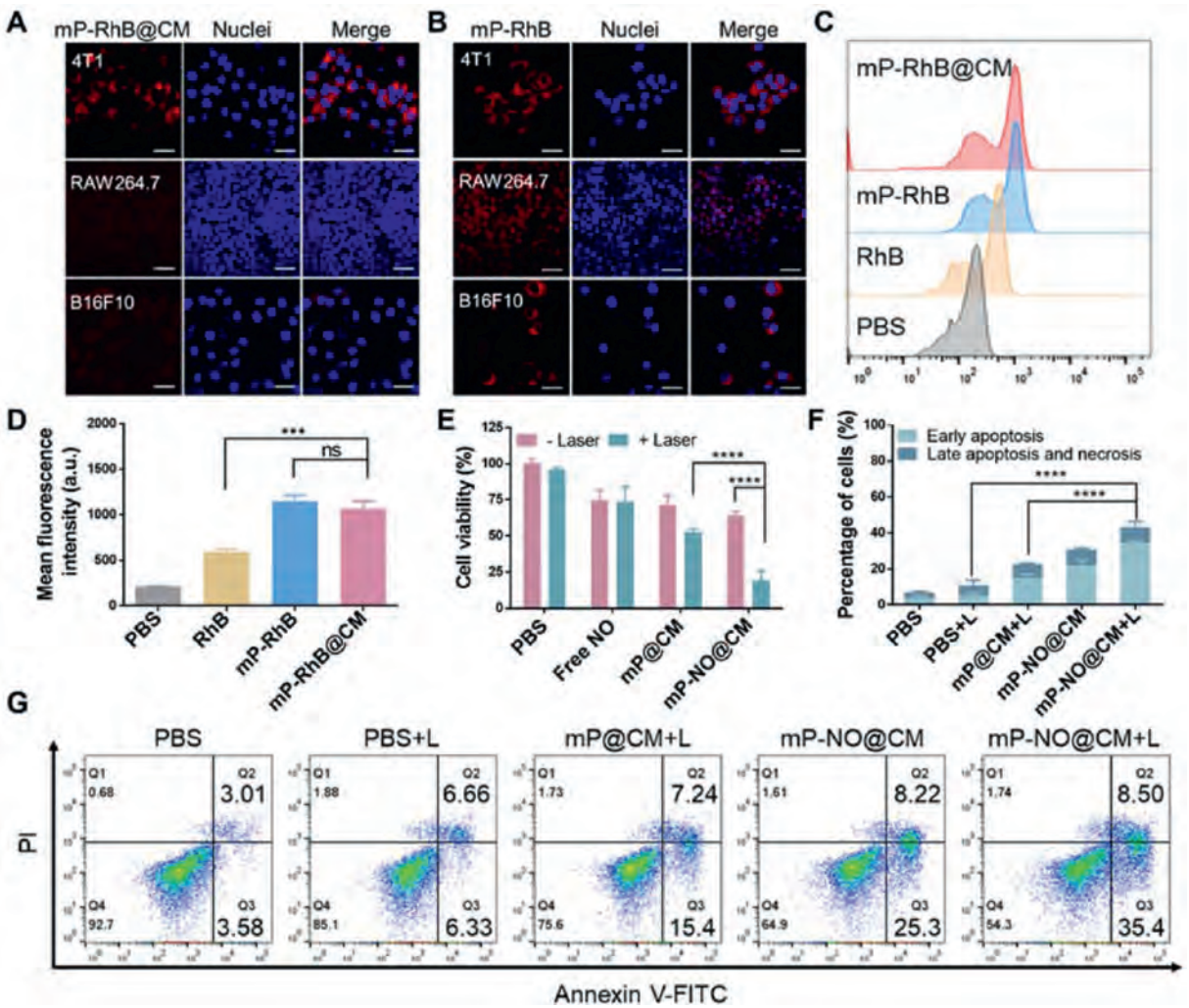

Figure 2 *In vitro* homologous targeting and synergistic antitumor efficacy. (A, B) Cell uptake of (A) mP-RhB@CM and (B) mP-RhB in 4T1, RAW264.7, and B16F10 cells. Scale bars, 40 μm. (C) Representative flow cytometry histogram of 4T1 cell uptake. (D) Quantitative analysis of cell uptake, $n = 3$. (E) Cell viability after different treatments, $n = 5$. (F) Quantitative analysis of cell apoptosis, $n = 3$. (G) Representative flow cytometry charts of cell apoptosis after different treatments. Data are presented as mean ± SD, $^{***}P < 0.001$, $^{****}P < 0.0001$. ns, not significant.

interstitial environment, and released completely after 4 h in a pH 5.0 medium, which mimicked the acidic lysosomes. The acid-responsive release property of NO allowed its efficient enrichment at tumor sites for further biological functions.

3.2. *In vitro homologous targeting and antitumor efficacy*

Based on previous studies[48,49], tumor cell membrane-coated preparations can promote homologous cell uptake and avoid phagocytosis by macrophages. Therefore, we observed the cell uptake of mP-RhB@CM and mP-RhB in 4T1, RAW264.7, and B16F10 cells, respectively. It was confirmed that the coating of 4T1 cell membranes could reduce the phagocytic clearance of macrophages and increase the internalization in 4T1 cells rather than B16F10 cells (Fig. 2A and B). However, there was no significant difference in the uptake of mP-RhB@CM and mP-RhB in 4T1 cells (Fig. 2C and D). This may be due to the natural adhesion properties of mPDA, which has abundant hydroxyl and amino groups and allows mP-RhB to show good cell uptake.

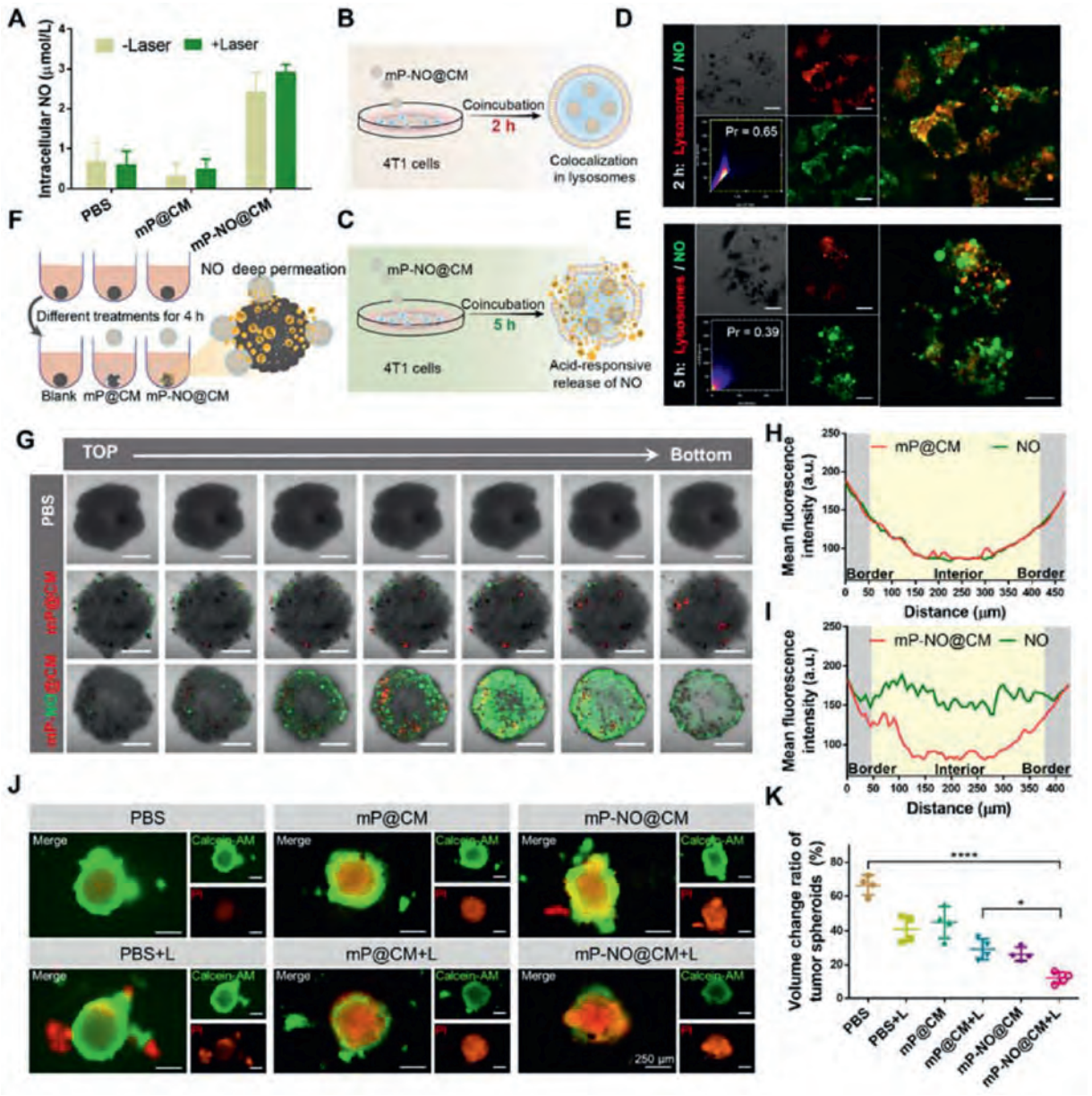

Figure 3 Intracellular NO release, intercellular NO penetration, and cytotoxicity on tumor spheroids. (A) Intracellular NO content, $n = 3$. (B, C) Illustration of the lysosomal escape of mP-NO@CM after incubation for (B) 2 h and (C) 5 h. (D, E) Lysosomal escape of NO after incubation for (D) 2 h and (E) 5 h. Lysosomes were stained with Lysotracker Red (red), and NO was labeled with DAF-FM DA (green). Scale bars, 10 μm. (F) Illustration of deep penetration of different preparations in 4T1 tumor spheroids. (G) Representative confocal images of tumor spheroids. mP@CM and mP-NO@CM were labeled with DiI (red), and NO was labeled with DAF-FM DA (green). Scale bars, 200 μm. (H, I) Radial fluorescence density map of the middle layer of the tumor spheroids after treated with (H) mP@CM or (I) mP-NO@CM. (J) Live/dead staining of tumor spheroids after different treatments. Scale bars, 250 μm. (K) Relative volume change ratio of tumor spheroids, $n = 4$. Data are presented as mean ± SD, $^{*}P < 0.05$, $^{****}P < 0.0001$.

In order to explore the antitumor effect of mP-NO@CM *in vitro*, MTT and apoptosis assays were performed. As shown in Fig. 2E, the mild PTT group (mP@CM + L, L meant laser irradiation) could kill nearly 45% of the tumor cells. In comparison, the mP-NO@CM + L group could kill about 80% of the tumor cells, highlighting the excellent auxiliary effect of NO. In the apoptosis assay, the mP@CM + L group only induced about 22.64% of the apoptosis rate, while that of the mP-NO@CM + L group was increased nearly 2-fold (Fig. 2F and G). These results strongly demonstrated that NO-assisted mild PTT exhibited enhanced antitumor efficacy by inducing more apoptosis and necrosis.

3.3. Evaluation of intracellular NO release and intercellular NO penetration

Based on the acid-responsiveness validated *in vitro*, the specific distribution of NO in tumor cells was further explored. First, the content of NO in 4T1 cells after different treatments was detected quantitatively by the Griess method. It was found that NO content was not significantly changed by PTT alone but increased greatly after being treated by mP-NO@CM due to the introduction of exogenous NO. Then, it could reach the effective therapeutic concentration of NO according to previous reports (>1 μmol/L, Fig. 3A) [41,42].

Furthermore, the NO fluorescent probe (DAF-FM DA) was used to trace its intracellular distribution, and the relative position of NO and lysosomes after 2 or 5 h of incubation was observed under CLSM (Fig. 3B and C). According to Fig. 3D, NO and lysosomes showed good colocalization with a Pearson correlation coefficient of 0.65 after 2 h. In contrast, the signal of NO was significantly misaligned with that of lysosomes after 5 h, with a decreased Pearson correlation coefficient of 0.39, further indicating that NO was released and escaped to the cytoplasm (Fig. 3E). From the weaker lysosomal signal, we speculated that the burst release of NO may destroy lysosomes and allow mP-NO@CM to escape from them. Supporting Information Fig. S11 verified that mP-RhB@CM was trapped in lysosomes after 6 h, and the intensity of lysosomes was still strong. This phenomenon proved that mPDA-based nanoparticles could not damage or

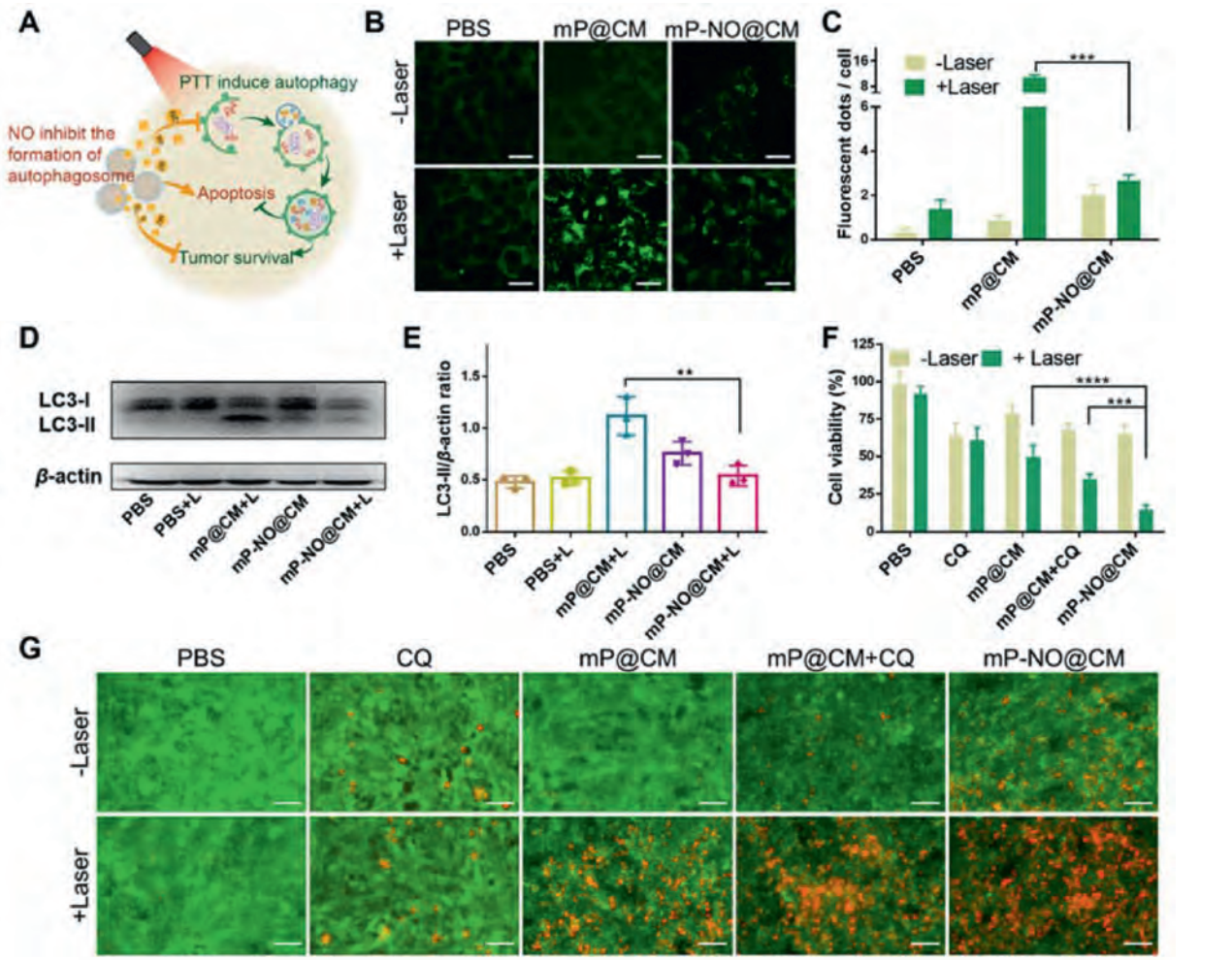

Figure 4 Inhibition of autophagy to sensitize mild PTT *in vitro*. (A) Schematic illustration of NO sensitizing PTT by inhibiting autophagy. (B) Representative confocal images of autophagosomes or autolysosomes (green fluorescent spots) after different treatments. Scale bars, 20 μm. (C) Count of fluorescent spots of Fig. 4B, $n = 3$. (D) Western blot analysis of LC3-I/II after different treatments. (E) Semi-quantitative analysis of LC3-II, $n = 3$. (F) Cell viability ($n = 5$) and (G) live/death staining of 4T1 cells treated with autophagy inhibitor (chloroquine, 25 μmol/L) combined with mild PTT. Scale bars, 200 μm. Data are presented as mean ± SD, $^{**}P < 0.01$, $^{***}P < 0.001$, $^{****}P < 0.0001$.

escape from the lysosomes. It also indirectly illustrated the auxiliary escape effect of loaded NO, which was a vital prerequisite for inhibiting autophagy.

To further investigate the diffusion of NO among tumor cells, 3D tumor spheroids of 4T1 were constructed (Fig. 3F). mP-NO@CM was labeled with DiI (red) and incubated with tumor spheroids for 4 h. Intercellular NO was stained with DAF-FM DA (green). The confocal images showed that mP-NO@CM was mainly trapped on the outer area of the tumor spheroid, while NO could deeply penetrate the central region (Fig. 3G−I). It implied that mP-NO@CM might compensate for the uneven distribution of photothermal agents leading to deep tumor survival, as NO could diffuse throughout the tumor and exert its antitumor effect directly.

The cytotoxicity of NO-assisted PTT on 4T1 tumor spheroids was evaluated for further study. As shown in live/dead staining (Fig. 3J), the red fluorescence intensity of dead cells increased after the treatment of mP@CM + L. Of note, it was further upregulated in the mP-NO@CM + L group, while the green fluorescence of live cells was relatively weakened. It illustrated the excellent adjuvant effect of NO on mild PTT. Furthermore, bright-field images were taken before and after administration to monitor the tumor spheroids' morphology and quantify the volume change. As shown in Fig. 3K and Supporting Information Fig. S12, the volume of tumor spheroids decreased to 29.1 ± 6.2% on Day 7 after the treatment of mP@CM + L. In comparison, with the auxiliary effect of NO in the mP-NO@CM + L group, the collapse of spheroids was further aggravated, and the final volume was reduced to 12.1 ± 3.4%. It confirmed that the deep penetration of NO contributed to the augmented antitumor effect and ameliorated the poor efficacy resulting from the persistence of deep-seated tumor cells.

3.4. *Inhibition of autophagy by NO in vitro*

According to the results of MTT and apoptosis assays, NO contributed enormously to enhancing the antitumor efficacy of mild PTT. The mechanism behind it deserved further investigation. According to previous studies[11], the obstacle limiting the efficacy of mild PTT lay in that tumor cells tended to initiate autophagy to avoid apoptosis (Fig. 4A). Therefore, inhibiting autophagy was promising for photothermal sensitization. Herein, we investigated the inhibitory effect of NO on autophagy. Monodansylcadaverine (MDC) staining (green fluorescent spots) and relative semi-quantitative counting both clarified that autophagy was significantly inhibited in the mP-NO@CM + L group

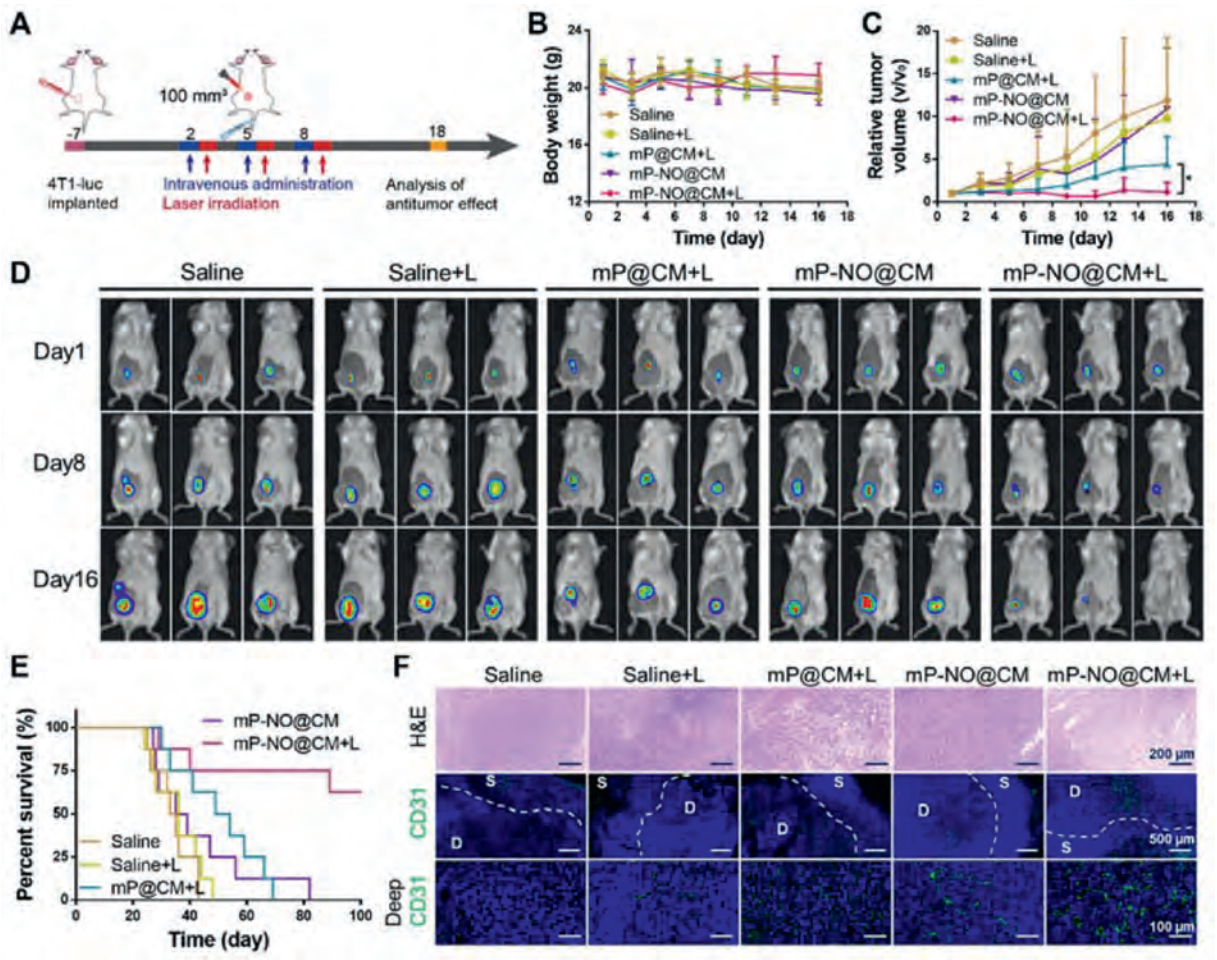

Figure 5 Antitumor effect in the 4T1 early-stage breast tumor model. (A) Schematic of the dosing schedule in the 4T1-luc breast tumor model. (B) Body weight monitoring, $n = 8$. (C) Relative tumor volume monitoring, $n = 8$. (D) Tumor growth trend monitored by bioluminescence imaging system, $n = 3$. (E) Survival curve to 100 days, $n = 8$. (F) Representative H&E staining and CD31 immunofluorescence staining of tumors, D means deep area, and S means superficial area. Data are presented as mean ± SD, $^*P < 0.05$.

compared with that in the mP@CM + L group (Fig. 4B and C). Besides, the results of Western blot showed that tumor cells treated with mP@CM + L exhibited the most accumulation of LC3-II, whereas there was a little LC3-II formed in mP-NO@CM ± L groups (Fig. 4D and E). The transition from LC3-I to LC3-II is generally considered a marker of autophagic activation. Taken together, NO effectively down-regulated the level of autophagy and was expected to sensitize mild PTT. The classical autophagy inhibitor chloroquine (CQ) was used as a positive control to further explore the effectiveness of combining autophagy inhibition with mild PTT. The results of the MTT assay showed that the viability of 4T1 cells was about 50% in the mP@CM + L group, which further reduced to about 35% after being treated with mP@CM + CQ + L and sharply decreased to about 15% after treatment with mP-NO@CM + L (Fig. 4F). It demonstrated that the inhibition of autophagy indeed enhanced the antitumor efficacy of mild PTT. NO showed a better adjuvant effect than CQ. Similarly, the live/dead staining results proved the conclusion again (Fig. 4G).

3.5. *Antitumor effect in the 4T1 early-stage breast tumor model*

The luciferase-expressing 4T1 (4T1-luc) tumor model was constructed, and the *in vivo* distribution of the nanoparticles was visualized by *in vivo* imaging. Compared with mP-Cy5.5, mP-Cy5.5@CM exhibited higher tumor targeting ability, attributed to the homologous targeting effect of the tumor cell membrane (Supporting Information Fig. S13).

The *in vivo* antitumor effect was first investigated in the 4T1 early-stage breast tumor model. When tumors grew to 100 mm^3, mice were randomly divided into five groups and given different treatments: saline, saline + L, mP@CM + L, mP-NO@CM, and mP-NO@CM + L. The 808 nm laser with 2 W/cm^2 power was used for 5 min per mouse. Specific schedules of drug administration and laser irradiation were shown in Fig. 5A. According to the results of weight monitoring, mP-NO@CM had no significant side effects on the mice, indicating its good biocompatibility (Fig. 5B). Tumor progression was monitored by measuring tumor volume and *in vivo* imaging (Fig. 5C and D). The above results revealed that the photothermal group (mP@CM + L) had a certain tumor-suppressing effect, but the mP-NO@CM + L group exhibited an even better antitumor efficacy. And the tumors disappeared gradually after three treatments. Furthermore, the median survival was prolonged to more than 100 days, much longer than that of the saline group (34 days) and mP@CM + L group (52 days) (Fig. 5E). These results indicated that the antitumor effect of mild PTT was limited, whereas the introduction of NO significantly enhanced it, confirming the good adjuvant role of NO. The hematoxylin-eosin (H&E) staining results also illustrated that mP-NO@CM + L could induce more tumor cell necrosis. Notably, there seemed to be more micro-vessels (Fig. 5F). For further verification, immunofluorescence staining of CD31 was

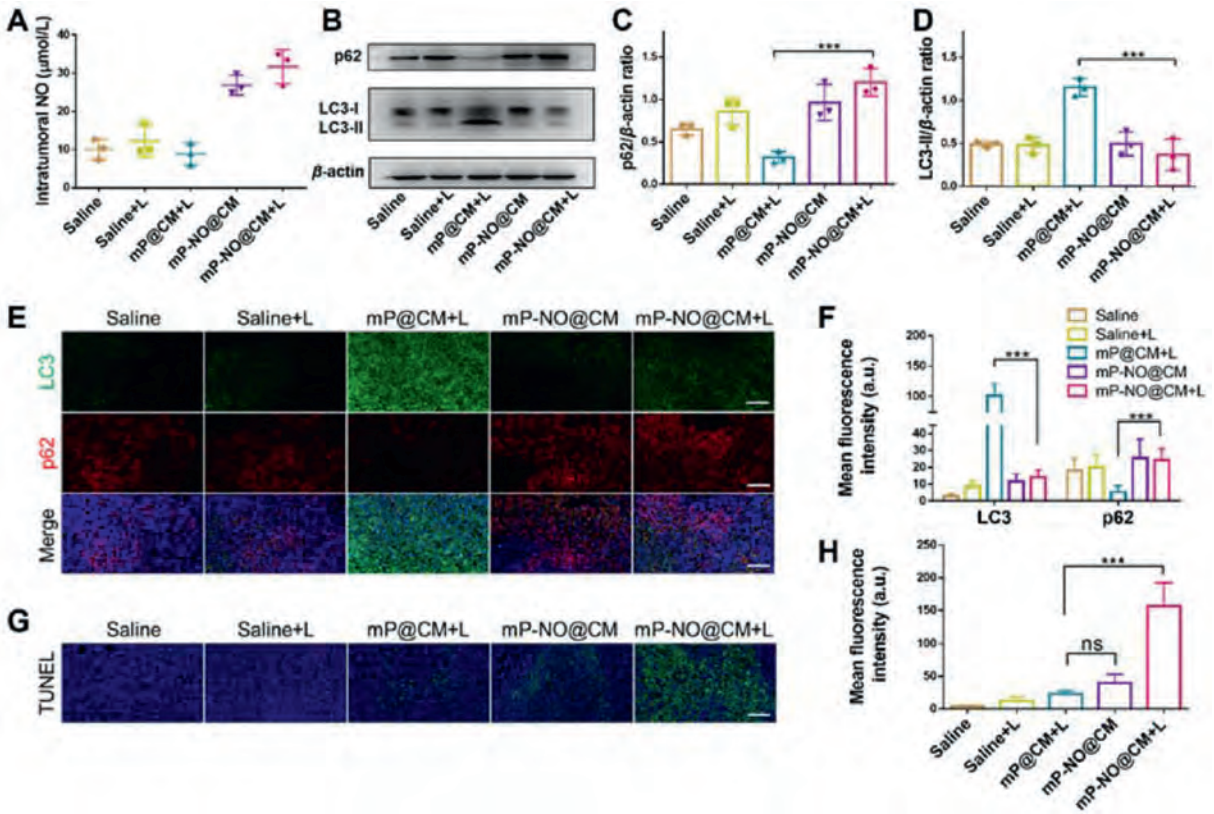

Figure 6 Inhibition of autophagy by NO *in vivo*. (A) Intratumoral NO content detected by Griess method, $n = 3$. (B) Western blot analysis of autophagy-related proteins p62 and LC3-I/II in tumors after different treatments. (C) Semi-quantitative analysis of p62, $n = 3$. (D) Semi-quantitative analysis of LC3-II, $n = 3$. (E) Representative images of immunofluorescence staining of LC3 and p62. Scale bars, 100 μm. (F) Semi-quantitative analysis of fluorescence of LC3 and p62, $n = 3$. (G) TUNEL staining. Scale bars, 100 μm. (H) Semi-quantitative analysis of TUNEL staining, $n = 4$. Data are presented as mean ± SD, $^{***}P < 0.001$. ns, not significant.

performed. Blood vessels were visible both superficially and deeply in the mP-NO@CM ± L group and were absent in the deep areas of the remaining three groups. It was thus inferred that NO can penetrate deep into the tumor and play a physiological role in promoting angiogenesis, which facilitates the intratumoral transport of nanomedicines.

3.6. *Inhibition of autophagy by NO in vivo*

To further explore the mechanism *in vivo*, we investigated the role of NO in regulating autophagy. The NO content in tumor lysates was first quantitatively detected using the Griess method. The NO content in mP-NO@CM + L groups was as high as 35 μmol/L, which was much higher than that in the other groups (Fig. 6A). It suggested that NO may contribute considerably to the strengthened antitumor effect. The results of the Western blot assay showed a marked elevation in LC3-II and a notable reduction in p62 after photothermal treatment (mP@CM + L), indicating the activation of autophagy. In sharp contrast, there was no obvious transition from LC3-I to LC3-II in the mP-NO@CM + L groups, and the level of p62 was slightly up-regulated (Fig. 6B−D). p62 is another autophagy-related protein whose expression is generally negatively correlated with the level of autophagy. Evidently, NO strongly inhibited autophagy *in vivo*, which helped to reduce the thermo-resistance of tumor cells. The results from immunofluorescence staining of LC3 and p62 further supported this conclusion (Fig. 6E and F). Additionally, TUNEL staining revealed significant apoptosis in the

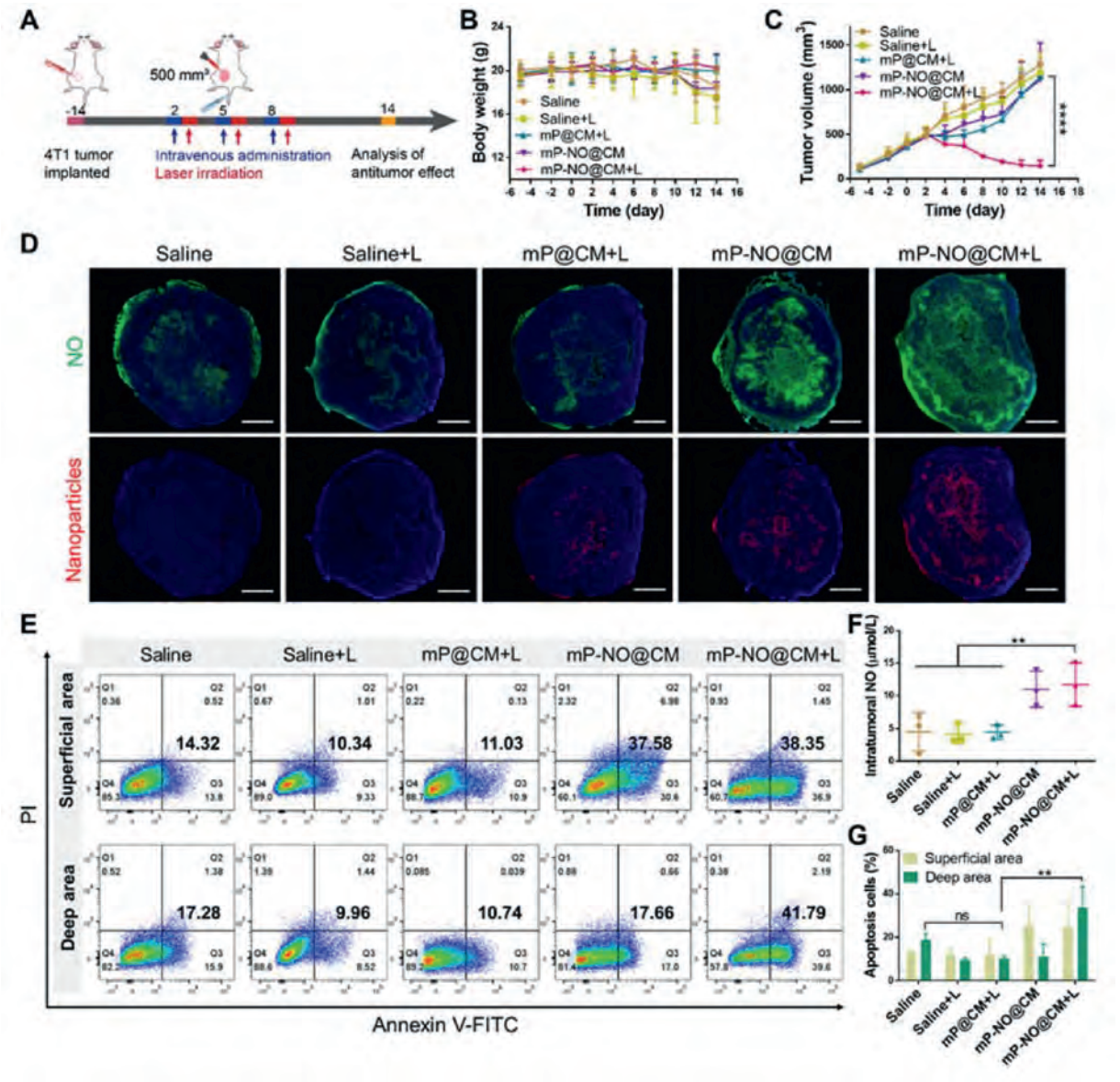

Figure 7 Antitumor effect in the 4T1 late-stage breast tumor model. (A) Schematic of the administration schedule in the late-stage tumor model. (B) Body weight monitoring, $n = 6$. (C) Tumor volume monitoring, $n = 6$. (D) Distribution of NO in frozen sections of tumors stained by DAF-FM DA (green), nanoparticles labeled by Cy3.5-NHS (red), and nuclei stained by DAPI (blue). Scale bars, 2000 μm. (E) Representative flow cytometry of apoptosis in the superficial and deep tumor areas, $n = 3$. (F) NO content in tumor tissues, $n = 3$. (G) Quantitative analysis of apoptosis of Fig. 7E, $n = 3$. Data are presented as mean ± SD, $^{**}P < 0.01$, $^{****}P < 0.0001$. ns, not significant.

mP-NO@CM + L group (Fig. 6G and H). Taken together, the released NO effectively inhibited photothermal-induced autophagy, thereby promoting tumor cell apoptosis and exerting excellent adjuvant efficacy.

3.7. Antitumor effect in the 4T1 late-stage breast tumor model

When the tumor volume reached 450−500 mm^3, the same treatments as the early-stage tumor model were performed. The schedule of administration and laser irradiation was depicted in Fig. 7A. The body weight fluctuated slightly during treatments, indicating the biocompatibility of the preparation (Fig. 7B). Through long-term monitoring of the tumor size, we found that the average tumor volume in the saline group exceeded 1300 mm^3 (Fig. 7C). Following photothermal treatment (mP@CM + L), tumor growth slowed down, but the tumor resumed rapid growth immediately after completion of treatments, with a final volume of more than 1100 mm^3. In sharp contrast, in the mP-NO@CM + L group, the tumor volume kept decreasing and ultimately remained below 130 mm^3. The above results fully demonstrated that NO could remarkably enhance the antitumor effect of mild PTT.

In order to investigate the penetration of NO, tumors were collected 12 h after intravenous administration and made into frozen sections. The intratumor NO was tracked by DAF-FM DA. It was evident that the red fluorescence of nanoparticles only partially penetrated the tumor and stayed localized, while the green fluorescence of NO was distributed deeply and even throughout the tumor (Fig. 7D). Notably, the mP-NO@CM + L group showed superior drug accumulation. We then performed CD31 staining and demonstrated that NO could promote the deep penetration of nanoparticles by promoting angiogenesis (Supporting Information Fig. S14). Subsequently, we analyzed cell apoptosis in the superficial and deep regions of tumors to assess the impact brought by the penetration of NO. Based on the sum of data in the Q2 quadrant (late apoptosis) and Q3 quadrant (early apoptosis), we found that the apoptosis rate was only induced by approximately 11% in both the superficial and deep regions after being treated with mP@CM + L, which was similar to that of the saline group (Fig. 7E−G). In comparison, the apoptosis rate was evidently elevated in the mP-NO@CM + L group (about 42% in the deep region and 38% in the superficial region). These findings strongly substantiated that the penetrated NO could kill deep-seated tumor cells directly, thus compensating for the insufficient photothermal effect inside the tumor. Besides, as presented in Fig. S14, the tissue structure of the tumor in the mP-NO@CM + L group was loose, with multiple regions of fragmented nuclei and apparent apoptosis. Additionally, the spleens in the mP-NO@CM + L group were similar in size to those of healthy mice. However, there was evident splenomegaly in the other groups, a typical indicator accompanying the progression of malignant tumors (Supporting Information Fig. S15A). By H&E staining, the splenic corpuscles disappeared in the first four groups but remained normal in the mP-NO@CM + L group (Fig. S15B). Meanwhile, heavy lung metastasis was observed in the first four groups. In contrast, the mP-NO@CM + L group showed few lung metastases, indicating NO-assisted therapy not only inhibited the progression of *in situ* tumors but also had the potential for anti-tumor metastasis.

3.8. Biocompatibility evaluation in vivo

The biological safety of drugs is an essential prerequisite for *in vivo* efficacy testing. Healthy mice were injected with saline and the same dose of mP-NO@CM as previously administered. Blood samples were collected for routine blood tests and blood biochemical tests. As shown in Supporting Information Fig. S16A, similar to the saline group, the numbers of red blood cells (RBC), white blood cells (WBC), the percentage of monocytes (Mon), and hemoglobin (HGB) in the mP-NO@CM group were within the normal range. Some representative indexes of liver and kidney function, such as alanine aminotransferase (ALT), aspartate aminotransferase (AST), blood urine nitrogen (BUN), and creatinine (CR), were also normal. Additionally, the two groups had no significant difference in H&E staining of the heart, liver, spleen, lung, and kidney (Fig. S16B). Taken together, mP-NO@CM showed no obvious toxicity and had good biocompatibility.

4. Conclusions

In summary, we designed a membrane-biomimetic NO nanogenerator that was efficiently loaded with NO donors and possessed good photothermal conversion performance. The mesoporous structure of mPDA created conditions for high drug loading, which was a prerequisite for adequate NO enrichment. We leveraged the unique property of NO as a highly reactive gas molecule. After targeted delivery to the tumor site, NO was released in an acid-responsive manner, penetrated into solid tumors, and induced deep tumor cell apoptosis, thereby compensating for the insufficient intratumor thermal effect. Moreover, NO potently inhibited the thermal-induced autophagy, which was pro-survival, and drove more tumor cells to apoptosis, thus sensitizing mild PTT. Consequently, this study expanded the application of NO-assisted gas therapy in treating solid tumors. As it has shown excellent antitumor effect in the late-stage breast tumor model, it is expected to be applied to other solid tumor models. Meanwhile, other potential mechanisms are also worthy of in-depth investigation except for inhibiting autophagy.

Acknowledgments

This work was financially supported by the National Key Research and Development Program of China (2024YFB3814603), the National Natural Science Foundation of China (82473866, 32471394), the Natural Science Foundation of Jiangsu Province (BK20251568, China), and the Key Research and Development Program Social Development Project of Jiangsu Province (BE2023845, China), Yangtze River Delta Science and Technology Innovation Community Joint Research Project (2023CSJZN0800, China), the Postdoctoral Fellowship Program (Grade B) of China Postdoctoral Science Foundation (GZB20250826), and Jiangsu Funding Program for Excellent Postdoctoral Talent (2025ZB747, Postdoctoral Fellow ID-392029, China).

Author contributions

Caixia Tan: Methodology, Writing − original draft, Formal analysis. Ming Yan: Methodology. Xinping Luo: Methodology. Honghao Sun: Methodology. Zhanwei Zhou: Writing − review & editing. Minjie Sun: Funding acquisition, Resources.

Conflicts of interest

The authors have no conflicts of interest to declare.

Appendix A. Supporting information

Supporting information to this article can be found online at https://doi.org/10.1016/j.apsb.2025.11.009.

References

1. Hirsch LR, Stafford RJ, Bankson JA, Sershen SR, Rivera B, Price RE, et al. Nanoshell-mediated near-infrared thermal therapy of tumors under magnetic resonance guidance. *Proc Natl Acad Sci U S A* 2003; **100**:13549−54.
2. Ouyang J, Xie A, Zhou J, Liu RC, Wang LQ, Liu HJ, et al. Minimally invasive nanomedicine: nanotechnology in photo-/ultrasound-/radiation-/magnetism-mediated therapy and imaging. *Chem Soc Rev* 2022; **51**:4996−5041.
3. Wang Y, Zhong HB, Yang J, Yao Y, Li L. Solvents/photo/pillar[5] arene triple responsive morphology and luminescence transformation from an amphiphilic dicyanostilbene-functionalized thiophene. *Chin Chem Lett* 2023;**34**:108452.
4. Wang Y, Wang D, Wang J, Wang CW, Wang J, Ding Y, et al. Pillar[5] arene-derived covalent organic materials with pre-encoded molecular recognition for targeted and synergistic cancer photo- and chemotherapy. *Chem Commun* 2022;**58**:1689−92.
5. Rastinehad AR, Anastos H, Wajswol E, Winoker JS, Sfakianos JP, Doppalapudi SK, et al. Gold nanoshell-localized photothermal ablation of prostate tumors in a clinical pilot device study. *Proc Natl Acad Sci USA* 2019;**116**:18590−6.
6. Sherar M, Liu FF, Pintilie M, Levin W, Hunt J, Hill R, et al. Relationship between thermal dose and outcome in thermoradiotherapy treatments for superficial recurrences of breast cancer: data from a phase III trial. *Int J Radiat Oncol Biol Phys* 1997;**39**:371−80.
7. Triantopoulou S, Efstathopoulos E, Platoni K, Uzunoglou N, Kelekis N, Kouloulias V. Radiotherapy in conjunction with superficial and intracavitary hyperthermia for the treatment of solid tumors: survival and thermal parameters. *Clin Transl Oncol* 2013;**15**:95−105.
8. Overchuk M, Weersink RA, Wilson BC, Zheng G. Photodynamic and photothermal therapies: synergy opportunities for nanomedicine. *ACS Nano* 2023;**17**:7979−8003.
9. Jordan A, Scholz R, Wust P, Fähling H, Felix R. Magnetic fluid hyperthermia (MFH): cancer treatment with AC magnetic field induced excitation of biocompatible superparamagnetic nanoparticles. *J Magn Magn Mater* 1999;**201**:413−9.
10. Gao G, Sun XB, Liang GL. Nanoagent-promoted mild-temperature photothermal therapy for cancer treatment. *Adv Funct Mater* 2021; **31**:2100738.
11. Zhang X, Du JF, Guo Z, Yu J, Gao Q, Yin WY, et al. Efficient near infrared light triggered nitric oxide release nanocomposites for sensitizing mild photothermal therapy. *Adv Sci* 2019;**6**:1801122.
12. Feng SP, Lu JY, Wang KL, Di DH, Shi ZN, Zhao QF, et al. Advances in smart mesoporous carbon nanoplatforms for photothermal-enhanced synergistic cancer therapy. *Chem Eng J* 2022;**435**:134886.
13. Li XS, Lovell JF, Yoon J, Chen XY. Clinical development and potential of photothermal and photodynamic therapies for cancer. *Nat Rev Clin Oncol* 2020;**17**:657−74.
14. Xiong YX, Wang W, Deng QY, Zhang ZJ, Wang Q, Yong ZT, et al. Mild photothermal therapy boosts nanomedicine antitumor efficacy by disrupting DNA damage repair pathways and modulating tumor mechanics. *Nano Today* 2023;**49**:101767.
15. Debnath J, Gammoh N, Ryan KM. Autophagy and autophagy-related pathways in cancer. *Nat Rev Mol Cell Biol* 2023;**24**:560−75.
16. Levy JMM, Towers CG, Thorburn A. Targeting autophagy in cancer. *Nat Rev Cancer* 2017;**17**:528−42.
17. Zhong ZY, Sanchez-Lopez E, Karin M. Autophagy, inflammation, and immunity: a troika governing cancer and its treatment. *Cell* 2016;**166**: 288−98.
18. Zhang YB, He X, Zhang YT, Zhao YP, Lu SY, Peng YJ, et al. Native mitochondria-targeting polymeric nanoparticles for mild photothermal therapy rationally potentiated with immune checkpoints blockade to inhibit tumor recurrence and metastasis. *Chem Eng J* 2021;**424**: 130171.
19. Zou Y, Li ML, Xiong T, Zhao XZ, Du JJ, Fan JL, et al. A single molecule drug targeting photosensitizer for enhanced breast cancer photothermal therapy. *Small* 2020;**16**:e1907677.
20. Lu JY, Song LM, Feng SP, Wang KL, Mao YL, Gao YK, et al. Nanozyme-mediated biocatalysis as a mitochondrial oxidative stress amplifier for tumor nanocatalytic immunotherapy. *Chem Eng J* 2024; **481**:148270.
21. Guo WH, Li ZH, Huang HL, Xu ZJ, Chen ZA, Shen GD, et al. VB12-sericin-PBLG-IR780 nanomicelles for programming cell pyroptosis *via* photothermal (PTT)/photodynamic (PDT) effect-induced mitochondrial DNA (mitoDNA) oxidative damage. *ACS Appl Mater Inter* 2022;**14**:17008−21.
22. Liu HM, Xu JM, Ye MJ, Zhang HB, Han LL, Wang JT, et al. Self-shrinking supramolecular nanoparticles syndicate energy suppression and NIR-II mild photothermal amplification of mitochondrial oxidative stress for breast cancer therapy. *Nano Res* 2024; **17**:4314−28.
23. Zhao LX, Cheng J, Liu D, Gong HX, Bai DC, Sun W. *Potentilla anserina* polysaccharide alleviates cadmium-induced oxidative stress and apoptosis of H9c2 cells by regulating the MG53-mediated RISK pathway. *Chin J Nat Med* 2023;**21**:279−91.
24. He XY, Fu JR, Lyu WY, Huang MY, Mo JS, Cheng YX, et al. Identification of Bulbocodin D and C as novel STAT3 inhibitors and their anticancer activities in lung cancer cells. *Chin J Nat Med* 2023;**21**: 842−51.
25. Santacruz-Gomez K, Melendrez R, Licerio-Ramírez M, Gallego-Hernandez AL, Pedroza-Montero M, Lal R. Alterations on Hela cell actin filaments induced by PEGylated gold nanorod-based plasmonic photothermal therapy. *J Nanopart Res* 2022;**24**:38.
26. Peng F, Liao MR, Qin R, Zhu SO, Peng C, Fu LL, et al. Regulated cell death (RCD) in cancer: key pathways and targeted therapies. *Signal Transduct Targeted Ther* 2022;**7**:286.
27. Taheriazam A, Abad GGY, Hajimazdarany S, Imani MH, Ziaolhagh S, Zandieh MA, et al. Graphene oxide nanoarchitectures in cancer biology: nano-modulators of autophagy and apoptosis. *J Control Release* 2023;**354**:503−22.
28. Wang MR, Tian BP, Shen J, Xu SL, Liu C, Guan L, et al. Bavachin induces apoptosis in colorectal cancer cells through Gadd45a *via* the MAPK signaling pathway. *Chin J Nat Med* 2023;**21**:36−46.
29. Amaravadi RK, Kimmelman AC, Debnath J. Targeting autophagy in cancer: recent advances and future directions. *Cancer Discov* 2019;**9**: 1167−81.
30. Ouyang ZJ, Gao Y, Shen SY, Jia BY, Yu HW, Wang H, et al. A minimalist dendrimer nanodrug for autophagy inhibition-amplified tumor photothermo-immunotherapy. *Nano Today* 2023;**51**:101936.
31. Zhou ZJ, Yan Y, Hu KW, Zou Y, Li YW, Ma R, et al. Autophagy inhibition enabled efficient photothermal therapy at a mild temperature. *Biomaterials* 2017;**141**:116−24.
32. Nan FL, Nan WL, Yu ZJ, Wang H, Cui XN, Jiang SS, et al. Polygalacin D inhibits the growth of hepatocellular carcinoma cells through BNIP3L-mediated mitophagy and endogenous apoptosis pathways. *Chin J Nat Med* 2023;**21**:346−58.
33. Wang Y, Liang XF, An J, Pu J, Meng YJ, Bai YQ, et al. H_2O_2-triggered CO release based on porphyrinic covalent organic polymers for photodynamic/gas synergistic therapy. *Chem Commun* 2024;**60**: 5864−7.
34. Wang ZX, Jin AL, Yang Z, Huang W. Advanced nitric oxide generating nanomedicine for therapeutic applications. *ACS Nano* 2023;**17**: 8935−65.
35. Zhang B, Qin YM, Yang L, Wu Y, Chen NY, Li MY, et al. A polyphenol-network-mediated coating modulates inflammation and vascular healing on vascular stents. *ACS Nano* 2022;**16**:6585−97.
36. Pelgrift RY, Friedman AJ. Nanotechnology as a therapeutic tool to combat microbial resistance. *Adv Drug Deliv Rev* 2013;**65**: 1803−15.

37. Shen ZQ, Zheng SQ, Fang YM, Zhang GY, Zhu C, Liu SY, et al. Overcoming the oxygen dilemma in photoredox catalysis: Near-infrared (NIR) light-triggered peroxynitrite generation for antibacterial applications. *Angew Chem Int Ed Engl* 2023;**62**:e202219153.
38. Li YC, Yoon B, Dey A, Nguyen V, Park JH. Recent progress in nitric oxide-generating nanomedicine for cancer therapy. *J Control Release* 2022;**352**:179−98.
39. Xu M, Zha HD, Chen JM, Lee SMY, Wang Q, Wang RB, et al. "Ice and fire" supramolecular cell-conjugation drug delivery platform for deep tumor ablation and boosted antitumor immunity. *Adv Mater* 2023;**35**:e2305287.
40. Zhu JL, Jiang XJ, Luo XY, Gao Y, Zhao R, Li JJ, et al. Discovery and bioassay of disubstituted β-elemene-no donor conjugates: synergistic enhancement in the treatment of leukemia. *Chin J Nat Med* 2023;**21**: 916−26.
41. Bai QC, Wang M, Liu JW, Sun XL, Yang PP, Qu FY, et al. Porous molybdenum nitride nanosphere as carrier-free and efficient nitric oxide donor for synergistic nitric oxide and chemo/sonodynamic therapy. *ACS Nano* 2023;**17**:20098−111.
42. Theivendran S, Gu ZY, Tang J, Yang YN, Song H, Yang Y, et al. Nanostructured organosilica nitric oxide donors intrinsically regulate macrophage polarization with antitumor effect. *ACS Nano* 2022;**16**: 10943−57.
43. Li XH, He SK, Ma BY. Autophagy and autophagy-related proteins in cancer. *Mol Cancer* 2020;**19**:12.
44. Sarkar S, Korolchuk VI, Renna M, Imarisio S, Fleming A, Williams A, et al. Complex inhibitory effects of nitric oxide on autophagy. *Mol Cell* 2011;**43**:19−32.
45. Ikeda-Imafuku M, Wang LLW, Rodrigues D, Shaha S, Zhao ZM, Mitragotri S. Strategies to improve the EPR effect: a mechanistic perspective and clinical translation. *J Control Release* 2022;**345**: 512−36.
46. Ding Y, Ma YX, Du C, Wang CW, Chen TT, Wang Y, et al. NO-releasing polypeptide nanocomposites reverse cancer multidrug resistance *via* triple therapies. *Acta Biomater* 2021;**123**:335−45.
47. Cheng H, He Y, Lu JY, Yan ZW, Song LM, Mao YL, et al. Degradable iron-rich mesoporous dopamine as a dual-glutathione depletion nanoplatform for photothermal-enhanced ferroptosis and chemodynamic therapy. *J Colloid Interface Sci* 2023;**639**:249−62.
48. Wan XY, Song LQ, Pan W, Zhong H, Li N, Tang B. Tumor-targeted cascade nanoreactor based on metal−organic frameworks for synergistic ferroptosis-starvation anticancer therapy. *ACS Nano* 2020;**14**: 11017−28.
49. Wang JP, Sun JY, Hu W, Wang YH, Chou TM, Zhang BL, et al. A porous Au@Rh bimetallic core−shell nanostructure as an H_2O_2-driven oxygenerator to alleviate tumor hypoxia for simultaneous bimodal imaging and enhanced photodynamic therapy. *Adv Mater* 2020;**32**:e2001862.
50. Peng L, Peng HR, Li W, Zhao DY. Monomicellar assembly to synthesize structured and functional mesoporous carbonaceous nanomaterials. *Nat Protoc* 2023;**18**:1155−78.
51. Bardestani R, Patience GS, Kaliaguine S. Experimental methods in chemical engineering: specific surface area and pore size distribution measurements-BET, BJH, and DFT. *Can J Chem Eng* 2019;**97**: 2781−91.
52. Sing KSW. Reporting physisorption data for gas/solid systems with special reference to the determination of surface area and porosity. *Pure Appl Chem* 1985;**57**:603−19.
53. Liu YL, Ai KL, Liu JH, Deng M, He YY, Lu LH. Dopamine-melanin colloidal nanospheres: an efficient near-infrared photothermal therapeutic agent for *in vivo* cancer therapy. *Adv Mater* 2013;**25**:1353−9.
54. Yang XY, Zhang CS, Song MJ, Zhang ZR, Zhou JP, Zhang HQ, et al. Enzyme-silenced nanosponges prolong intratumoral lifetime to facilitate intercellular relay drug delivery and treatment efficacy. *ACS Nano* 2023;**17**:23568−83.
55. Xu HW, Zhang Y, Zhang HT, Zhang YR, Xu QQ, Lu JY, et al. Smart polydopamine-based nanoplatforms for biomedical applications: state-of-art and further perspectives. *Coord Chem Rev* 2023; **488**:215153.